Composites Communications 68 (2026) 102982

Contents lists available at ScienceDirect

Composites Communications

journal homepage: www.elsevier.com/locate/coco

White-light-emitting piezoelectric biocomposite nanofiberss

Juan Li [a], Chu Pan [a], Biyao Huang [a], Zhipei Xia [a], Jiashun Wen [a], Xuhang Lu [a], Weiqing Yang [b,*], Jun Lu [a,**,1]

[a] Key Laboratory of Advanced Technologies of Materials, Ministry of Education, School of Chemistry, Southwest Jiaotong University, Chengdu, 610031, Sichuan, China
[b] Research Institute of Frontier Science, Southwest Jiaotong University, Chengdu, 610031, Sichuan, China

ARTICLE INFO

Keywords:
Multifunction integrated composites
PHBV
Carbon quantum dots
$CuInS_2$ quantum dots
Electrospinning
Electrical properties

ABSTRACT

Herein, white-light-emitting quantum dots (WLQDs) are incorporated into biodegradable poly(3-hydroxybutyrate-co-3-hydroxyvalerate) (PHBV) to construct white-emissive piezoelectric nanofibrous membranes. The eco-friendly WLQDs are obtained by physically mixing blue-emissive carbon quantum dots (B-CQDs) and red-emissive copper indium disulfide ($CuInS_2$) quantum dots (R-CISQDs), thereby enabling white-light emission without the need for complex multicomponent energy transfer regulation. The aligned WLQDs/PHBV nanofibers are produced by electrospinning using a high speed drum collection method. Appropriate addition of WLQDs can improve fiber alignment and increase the orientation of internal PHBV crystalline domains. These structural features are considered to facilitate dipole arrangement in PHBV matrix to enhance piezoelectric response. The WLQDs/PHBV-based piezoelectric device exhibits a short-circuit current density of 1 μA cm^{-3} and an open-circuit voltage density of 26 V cm^{-3}, corresponding to 2.5 times the output of neat PHBV. And stable output is maintained over more than 10,000 cycles. The device is further used in motion sensing applications, where the real-time sensitive detection of facial movement, joint motion, and ambient vibration signals is achieved. The WLQDs/PHBV nanofibers are biodegradable under composting conditions, which may reduce environmental impact after use. This work proposes for the first time a bionanofiber material that integrates white-light emission and piezoelectric response, which may diversify niche applications in emerging transient wearable optoelectronic devices.

1. Introduction

White-light-emitting materials are key functional materials in portable light sources [1–3], smart textiles [4], and information security [5,6]. Recently, significant progress has been achieved in white-light-emitting materials. Lead-free perovskite phosphors have shown efficient broadband white-light emission and tunable luminescence properties, highlighting their potential for advanced lighting and optical applications [7,8]. Nevertheless, integrating these high-performance white-light-emitting materials into flexible, biodegradable, and wearable platforms remains challenging. Common preparation methods typically involve dispersing inorganic phosphorescent powders into a rigid polymer matrix through coating or related casting processes. These materials often exhibit limited mechanical flexibility, poor processability, and restricted biocompatibility. As a result, their application in curved and wearable devices is limited [9]. Electrospun nanofibers offer a viable alternative due to their high specific surface area, interconnected porous structure, and good mechanical adaptability [10–19]. The fiber architecture enables the emitting material to be spatially confined within the fiber array. This confinement helps suppress aggregation-induced quenching and reduces undesired energy transfer by regulating the distance between emitters. Electrospun light-emitting nanofibers have therefore been explored in flexible lighting, stimulus-responsive sensing, and anti-counterfeiting [5,20–22].

Despite these advantages, current white-light-emitting electrospun nanofibers still face several challenges. Most systems rely on petroleum-based polymers. These materials do not meet the requirements for sustainable and biodegradable electronics. Furthermore, their functionality is often limited to light emission. Integration with additional functions, such as piezoelectric sensing or energy harvesting, remains rare.

* Corresponding author.
** Corresponding author.
E-mail addresses: wqyang@swjtu.edu.cn (W. Yang), junluprc@hotmail.com (J. Lu).
[1] Other used names Jun Lv and Jun Lyu.

https://doi.org/10.1016/j.coco.2026.102982
Received 20 September 2026; Received in revised form 25 October 2026; Accepted 26 October 2026
Available online 27 October 2026
2452-2139/© 2026 Elsevier Ltd. All rights are reserved, including those for text and data mining, AI training, and similar technologies.

Meanwhile, the emissive components are typically based on organic dyes or perovskite materials. These materials may exhibit limited stability, potential toxicity concerns, or complex synthesis processes, which restrict their use in wearable and bio-integrated systems. In the field of flexible piezoelectric materials, conventional piezoelectric ceramics exhibit high piezoelectric coefficients but suffer from intrinsic brittleness [23,24]. Piezoelectric polymers, such as poly(vinylidene fluoride) (PVDF), offer improved flexibility but are non-degradable, raising concerns regarding environmental impact and long-term biosafety in epidermal contact devices [25,26]. Poly(3-hydroxybutyrate-co-3-hydroxyvalerate) (PHBV) is a biodegradable aliphatic copolyester derived from renewable resources. It has been reported to exhibit piezoelectric behaviour, along with good biocompatibility and complete degradability [27,28]. These properties make PHBV a potential candidate for sustainable piezoelectric systems. However, its piezoelectric output remains relatively low, and it lacks intrinsic luminescent functionality. These limitations hinder its application in multifunctional wearable optoelectronic devices.

To achieve efficient, stable, and biocompatible white-light emission, a composite system is constructed by blending blue-emissive carbon quantum dots (B-CQDs) with red-emissive copper indium disulfide ($CuInS_2$) quantum dots (R-CISQDs) at a controlled ratio. CQDs are characterized by high physical and chemical stability with low cytotoxicity [29–36]. CISQDs are known for their relatively narrow emission bandwidth and good biocompatibility [37,38]. When an appropriate proportion is applied, an emission profile close to standard white light can be achieved. Compared with conventional inorganic phosphors, the use of quantum dots provides enhanced photostability and a broader emission spectrum. White-light-emitting quantum dots (WLQDs) are not only used as luminescent centers, but also introduced as nanoscale functional fillers. The orientation and specific surface area of electrospun PHBV nanofibers can be regulated, and the piezoelectric response is consequently enhanced. In addition, the effects of WLQDs on fiber morphology, crystalline structure, optical properties, and piezoelectric properties are systematically evaluated. Their application in flexible wearable devices and human motion sensing is further demonstrated.

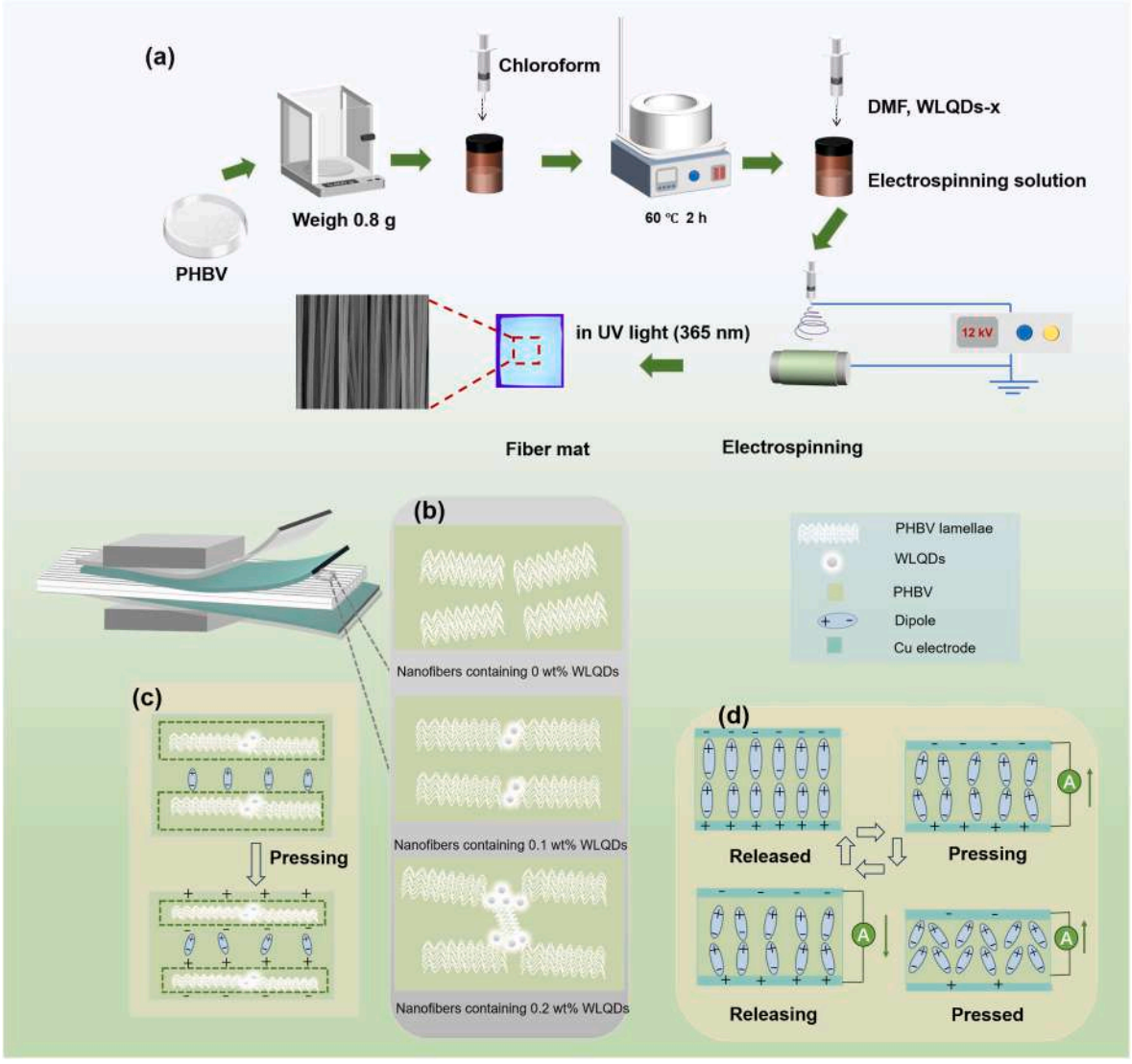


Fig. 1. (a) Schematic illustration of the fabrication process of WLQDs-x electrospun fibers. (b) Schematic diagram illustrating the role of WLQDs in enhancing the crystalline lamellae orientation of PHBV within electrospun fibers. (c) Illustration of WLQDs-induced dipole alignment and interfacial polarization within the PHBV matrix. (d) Working mechanism of the WLQDs/PHBV-based bio-piezoelectric nanogenerator under mechanical deformation, including the processes of charge generation, separation, and transport.

2. Experimental section

2.1. Materials and reagents

Poly(3-hydroxybutyrate-co-3-hydroxyvalerate) (PHBV, ENMAT Y1000; 1mol.% 3HV; Mη: 460,000) was provided by Ningbo TianAn Biologic Materials Co., Ltd, Zhejiang, China. Red-emissive copper indium disulfide ($CuInS_2$) quantum dots (R-CISQDs) were provided by Nanjing Janas New-Materials Co., Ltd, Jiangsu, China. The excitation wavelength range is 400-450 nm, and the emission wavelength range is 640 ± 5 nm. Blue-emissive carbon quantum dots (B-CQDs) were provided by Nanjing Janas New-Materials Co., Ltd, Jiangsu, China. The excitation wavelength range is 370-410 nm, and the emission wavelength range is 460 ± 5 nm. N, N-Dimethylformamide (DMF, AR) and Chloroform (AR) were both purchased from Chengdu Kelong Chemical Co., Ltd, Sichuan, China.

2.2. Fabrication of WLQDs/PHBV electrospun nanofibers

The fabrication process of WLQDs/PHBV nanofibers by electrospinning is shown in Fig. 1a. Firstly, 9 mL of chloroform was added to 0.8 g of PHBV powder. The mixture was heated in a 60 °C water bath in a closed environment for 2 h. After removal and cooling, 1 mL of DMF was added into PHBV/chloroform and thoroughly dispersed to obtain a uniform PHBV/chloroform/DMF solution. Next, a 3 mg/mL solution of R-CISQDs was mixed with a 10 mg/mL solution of B-CQDs in a 1:1 vol ratio to prepare the WLQDs solution. Finally, 0.1 wt% WLQDs were added to the PHBV/chloroform/DMF solution and vigorously stirred for 1 h to obtain the WLQDs/PHBV/chloroform/DMF spinning solution. In addition, we prepared a spinning solution containing 0.2 wt% WLQDs and a spinning solution without quantum dots using the same method. Once the spinning solution was prepared, it was loaded into a flat tip syringe with an inner diameter of 0.41 mm. The collection apparatus utilised a rotating drum, with an external voltage of 12 kV, a collection distance of 20 cm, and a flow rate of 10 μL/min. A high rotational speed of 4000 r/min was maintained to obtain highly oriented fibers. WLQDs/PHBV nanofibers containing different concentrations of WLQDs are denoted as WLQDs-x, where x represents the mass fraction of WLQDs. Nanofibers with WLQDs concentrations of 0 wt%, 0.1 wt%, and 0.2 wt% in the PHBV matrix are expressed as WLQDs-0, WLQDs-1, and WLQDs-2, respectively.

2.3. Characterization of materials

B-CQDs in DMF solution, R-CISQDs in chloroform solution, WLQDs solution, and WLQDs in the PHBV substrate were characterized using a transmission electron microscope (TEM) JEOL-2100F. Among them, B-CQDs, R-CISQDs, and WLQDs can be observed after deposition and drying on copper grids. To prevent the biomaterials from being damaged under high voltage, WLQDs in the PHBV substrate need to be embedded in epoxy resin for observation. The morphology of WLQDs-x fibers was characterized by using a scanning electron microscope (SEM) JSM-6330F. Since the conductivity of biomaterials is typically very poor, all samples require gold spraying before characterization. The XRD data of all samples of WLQDs-x were collected simultaneously using an X-ray diffractometer PANalytical X'pert PRO. The pole figures of WLQDs-x fiber membranes were detected using a PANalytical Empyrean Series 2 X diffractometer. When testing the pole figures of fiber membranes, the diffraction angles of different crystal planes were determined according to XRD. Then, a specific crystal plane was selected to test the lattice orientation of WLQDs-x fibers. During the test, the polar angle θ was maintained between 0° and 75°, the rotational azimuth angle Φ was maintained between 0° and 360°, and the step size of both was 5°. The attenuated total reflection Fourier transform infrared spectroscopy (ATR-FTIR) of WLQDs-x fibers was obtained by a Nicolet iS50 spectrometer with a scanning range of 4000 - 400 cm^{-1} and a resolution of 0.25 cm^{-1}. The crystallinity of WLQDs-x fibers was determined using a TA-Q20 differential scanning calorimeter (DSC). Each sample was heated from 30 °C to 230 °C under a nitrogen atmosphere at a heating rate of 10 °C/min. The crystallinity X_c of the samples was calculated using the following formula:

$$X_c = \Delta H_m \,/\, \left(\Delta H_m^0 \times \omega(\mathrm{PHBV})\right) \quad (1)$$

where ΔH_m is the measured heat of melting, ω(PHBV) is the mass fraction of PHBV in a composite sample, and ΔH_m^0 is chosen as 146.6 J/g for the heat of fusion of 100% crystalline PHBV due to the low HV content of PHBV in our study [39]. Photoluminescence (PL) emission spectra were recorded using an Edinburgh Instruments FLS980 spectrofluorometer equipped with a 450 W xenon lamp. The CIE 1931 chromaticity coordinates were determined from the corresponding PL emission spectra using the built-in chromaticity analysis module of the F980 software. The room-temperature absolute PL quantum yields (QYs) were measured using a calibrated integrating sphere attached to the FLS980 spectrofluorometer. The absolute QYs were determined as the ratio of the number of emitted photons to the number of absorbed excitation photons.

2.4. Fabrication of bio-PENGs

The WLQDs-x-based bio-nanogenerator is a sandwich structure comprising a WLQDs-x fiber membrane, copper (Cu) electrodes, and polyurethane (PU) tape, as shown in Fig. S1(a). First, the WLQDs-x fiber membrane was cut into 2×2 cm squares, and multiple square fiber membranes were stacked to achieve a thickness of 0.35 mm. Next, copper electrodes, slightly smaller than the fiber membranes, are attached to both sides of the stack. Finally, a layer of PU tape is applied to the upper and lower surfaces of the copper electrodes to serve as a protective layer, thereby preventing wear and corrosion from affecting the test results.

2.5. Test of bio-PENGs

The piezoelectric properties of WLQDs-x-based bio-piezoelectric nanogenerator (bio-PENG) were measured through repeated impact testing. As shown in Fig. S1(a), the test system utilised a linear motor (model NTIAG HS01-37×166) as the impact source, with a Keithley 6514 electrometer and a Stanford Research SR570 low-noise current amplifier for electrical signal acquisition. To minimise the generation of triboelectric charges during testing, acrylic panels made of the same material as the impact head have been fitted on both sides of the bio-nanogenerator. Switching polarity tests were also conducted to confirm the electrical outputs were truly generated by the assembled bio-PENGs, rather than originating from the measurement system or the environment. As shown in Fig. S1(b), the bio-PENG was connected to the circuit in both forward and reverse directions. The resulting inversion of the current and voltage output signals serves as evidence that the signals are piezoelectric in nature [40,41].

2.6. Monitoring of human physiology

The human sensing experiments involved only the first author (Juan Li) as the participant. All experimental procedures involving human participation complied with the applicable institutional and local ethical requirements. The informed consent was obtained from the participant prior to the experiments.

3. Results and discussion

WLQDs were incorporated into a PHBV spinning solution. WLQDs/PHBV nanofiber membranes with uniform fiber diameters and a high degree of alignment were fabricated via electrospinning (Fig. S2). Bright

white emission was observed under 365 nm ultraviolet irradiation (Fig. 1a). The incorporation of an appropriate amount of WLQDs was found to reduce the diameter of PHBV fibers and improve the orientation of both PHBV nanofibers and lamellar crystals. As a result, the piezoelectric performance was enhanced.

To provide a possible explanation for these structural changes, a schematic mechanism is proposed in Fig. 1b. During electrospinning, the rapid evaporation of volatile solvents, such as chloroform, may affect the dispersion state of WLQDs, thereby influencing the oriented growth of PHBV crystals. At an appropriate loading (0.1 wt%), the well dispersed WLQDs may promote the preferential orientation growth of PHBV crystalline lamellae. In contrast, an excessive WLQDs loading (0.2 wt%) may lead to nanoparticle aggregation, which can partially disrupt the preferential orientation growth and consequently induce the misorientation growth of PHBV crystalline lamellae. This proposed mechanism is intended to provide a possible explanation for the experimentally observed structural evolution and enhanced piezoelectric response of the WLQDs/PHBV nanofibrous membranes.

The piezoelectricity of PHBV primarily stems from the intrinsic dipole moments formed by the polar groups such as carbonyl (C=O) groups within its molecular chains [42]. During electrospinning, the strong stretching force generated by the high-speed collector induces the orientation of PHBV molecular chains along the fiber axis, accompanied by the alignment of C=O dipoles. In the absence of external mechanical stimulation, the ordered dipoles remain electrically balanced due to symmetry, resulting in negligible macroscopic polarization. When the compressive stress is applied perpendicular to the fiber direction, the deformation of the molecular chains disturbs the original dipole arrangement and breaks the charge symmetry, generating polarization charges (Fig. 1c). Under dynamic mechanical loadings, the dipole orientation changes dynamically. Consequently, the polarization level of the material is dynamically changed, and the free charges are dynamically induced on the electrode surfaces. These charges flow between the electrodes, thus continuously producing the instantaneous piezoelectric output signals (Fig. 1d).

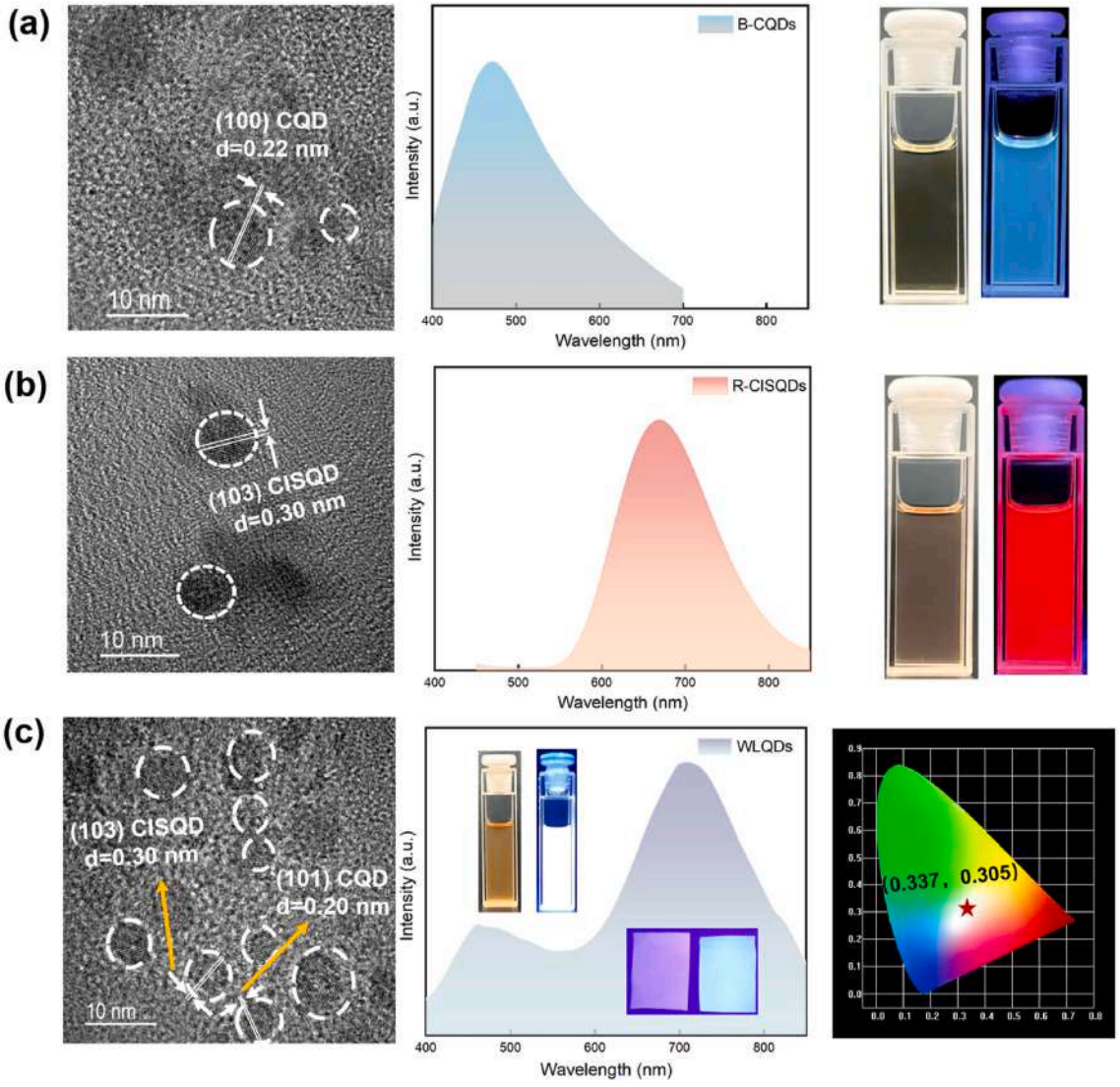


Fig. 2. (a) TEM image and PL emission spectra of B-CQDs in DMF, along with digital photographs under natural light (left) and UV illumination (right, $\lambda_{ex} = 365$ nm). (b) TEM image and PL emission spectra of R-CISQDs in chloroform, along with digital photographs under natural light (left) and UV illumination (right, $\lambda_{ex} = 365$ nm). (c) TEM image, PL emission spectra and CIE chromaticity diagram of WLQDs in solution. In PL spectra, the upper-left inset shows the digital photographs of WLQDs solution under natural light (left) and UV illumination (right, $\lambda_{ex} = 365$ nm), and the bottom-right inset shows the digital photographs of pristine PHBV (left) and WLQDs/PHBV (right) nanofiber membranes under UV illumination ($\lambda_{ex} = 365$ nm).

3.1. Optical properties of WLQDs and WLQDs-x fibers

This work uses a physical mixing method to prepare the WLQDs solution. A 10 mg/mL solution of B-CQDs was uniformly mixed with a 3 mg/mL solution of R-CISQDs in a 1:1 vol ratio to obtain the WLQDs solution. TEM characterisation of the three quantum dot solutions revealed distinct lattice fringes in local regions, with no obvious agglomeration observed (Fig. 2). The crystal plane spacing of B-CQDs is 0.22 nm, corresponding to the (100) crystal plane (Fig. 2a). The CIE chromaticity coordinates are determined to be (0.230, 0.268) (Fig. S3a), and the quantum yield (QY) is calculated as 26.83% (Fig. S4a). Its fluorescence emission spectrum exhibits an emission peak at 470 nm, corresponding to the blue emission region. R-CISQDs exhibit an emission peak at 660 nm, with the crystal plane spacing of 0.30 nm, corresponding to the (103) crystal plane (Fig. 2b), CIE chromaticity coordinates of (0.632, 0.345) (Fig. S3b), and a high QY of 61.14% (Fig. S4b). Fig. 2c shows the TEM image and optical properties of the mixed WLQDs solution. It can be seen that B-CQDs and R-CISQDs retain their respective morphological characteristics in the blended system, exhibiting uniform mixing without significant aggregation. Lattice fringes can be clearly observed in the TEM images, with a crystal plane spacing of 0.30 nm corresponding to the (103) crystal plane of R-CISQDs, and a crystal plane spacing of 0.20 nm corresponding to the (101) crystal plane of B-CQDs. The fluorescence emission spectrum in Fig. 2c shows that WLQDs exhibit two characteristic emission peaks simultaneously at around 470 nm and 660 nm, corresponding to the contributions of B-CQDs and R-CISQDs, respectively. These results indicate that no new luminescent species were formed in the mixed system, and no significant electronic coupling or chemical bonding has occurred within system. B-CQDs and R-CISQDs retained their respective independent luminescent properties during the physical blending process. By optimizing the concentration ratio of the two components, the blue and red emission bands together contribute to the overall emission, producing white-light emission. The CIE chromaticity coordinates of the WLQDs are (0.337, 0.305), which are very close to those of standard white light (0.33, 0.33), with a quantum yield (QY) of 38.4% (Fig. S4c). The quantum yield lies between those of red and blue quantum dots, reflecting the combined influence of multiple factors. Although no significant spectral shifts are observed, the partial spectral overlap suggests the possible presence of non-radiative energy transfer processes, such as Förster resonance energy transfer. In addition, local enrichment during mixing may reduce the average interparticle distance, enhancing energy coupling while potentially introducing non-radiative recombination pathways. Based on the luminescent properties of WLQDs, the prepared WLQDs were doped into the PHBV electrospinning precursor solution, and WLQDs/PHBV composite nanofiber membranes were obtained by electrospinning. To observe the distribution of WLQDs within the PHBV, the WLQDs-1 nanofibers were embedded in epoxy resin to prevent the biomaterial from being damaged under high voltage. TEM images (Fig. S3d) revealed that WLQDs are well dispersed within the local regions of PHBV. Distinct lattice striations were observed in individual dispersed WLQDs, confirming that the incorporated WLQDs were indeed attached to the PHBV. Furthermore, under irradiation with a 365 nm UV lamp, the composite fiber membrane exhibited uniform white-light emission (Fig. 2c). The WLQDs-1 fiber membrane exhibited a quantum yield (QY) of 19.94%, whilst the WLQDs-2 fiber membrane exhibited a QY of 10.27% (Fig. S4 d-e), which is lower than the quantum yield in the solution state. This was attributed to the rapid evaporation of the solvent during electrospinning, which caused local aggregation of WLQDs within the fibers. Such aggregation reduced the average distance between WLQDs and potentially enhanced the energy coupling interactions. In addition, extra non-radiative recombination pathways may have been introduced during the electrospinning process, leading to increased energy dissipation and an overall decrease in quantum yield.

This study did not employ the traditional strategy of mixing red, green, and blue primary-color quantum dots, but instead opted for the direct compounding of blue and red secondary color quantum dots to construct a white-light emission system. This approach is based on the principle of colour complementarity: according to the CIE chromaticity diagram, the line connecting the color coordinates of B-CQDs (0.230, 0.268) and R-CISQDs (0.632, 0.345) passes through the white-light region (Fig. S3c). When the two types of quantum dots are mixed in an appropriate concentration ratio, blue emission and red emission together produce white emission that closely approximates the coordinates of pure white light. This confirms the feasibility of building a white light system based on a dual-color complementary emission strategy. Compared to ternary systems, this strategy effectively avoids complex cascade energy transfer between multiple components, reduces unnecessary energy loss, and achieves precise white light tuning whilst simplifying the preparation process.

3.2. Structural characterization, mechanical properties, and degradation behavior of WLQDs-x fibers

Electrospinning provides a versatile platform for fabricating piezoelectric nanofibers with controllable morphology and molecular orientation. The electric-field-induced stretching and rapid solvent evaporation promote chain alignment and fiber solidification, while fiber diameter, fiber morphology, and fiber orientation directly influence the stress transfer and dipole polarization [43–48]. Therefore, optimizing electrospinning parameters is essential for achieving uniform and highly oriented nanofibers with enhanced piezoelectric performance [49].

The electrospinning parameters of PHBV were optimized before the incorporation of WLQDs. After the addition of WLQDs, fibers with smooth and uniform morphology were consistently obtained. Using a high speed rotating drum collector, the resulting fiber morphology, diameter distribution, and crystalline orientation are presented in Fig. 3a–c. As shown in the low and high magnification SEM images, the electrospun WLQDs-x fibers exhibit a good aligned, continuous fibrous structure. The diameter distribution analysis reveals that the average fiber diameter of neat PHBV (WLQDs-0) is 0.835 μm. With the incorporation of a low content of WLQDs (WLQDs-1), the average diameter decreases to 0.709 μm, accompanied by a narrower distribution. This reduction may be associated with the enhanced electrostatic stretching arising from increased solution conductivity. At higher WLQDs loading (WLQDs-2), the average diameter is 0.787 μm, which is likely related to the increased solution viscosity that restricts jet stretching during electrospinning. The (020) reflection was selected for XRD pole figure analysis because it exhibits the highest diffraction intensity and a well-resolved peak in the XRD patterns, providing reliable information for evaluating the crystallographic orientation of PHBV crystals (Fig. 3d). The (020) pole figures show a symmetric relative intensity distribution, indicating the preferential orientation of PHBV crystals along the fiber direction. After incorporation of WLQDs, the maximum relative intensity increased, with WLQDs-1 exhibiting the highest value of 1.58, indicating the highest degree of crystallographic orientation among the investigated samples.

To further investigate the crystal structure, XRD patterns of WLQDs-x samples were analyzed (Fig. 3d). With increasing WLQDs content, the diffraction peak intensity decreases slightly, while the peak positions remain unchanged at $2\theta \approx 13.4^\circ$ and 16.8°. This suggests that no new crystalline phase is formed and that WLQDs are physically incorporated into the PHBV matrix. Differential scanning calorimetry (DSC) analysis (Fig. 3e) shows that all samples exhibit crystallinity values above 60%. A gradual decrease in crystallinity is observed with increasing WLQDs content, while the melting temperature remains nearly constant at approximately 177 °C. This may be attributed to the presence of WLQDs, which can hinder polymer chain packing and restrict crystal growth. The Fourier transform infrared (FTIR) spectra of WLQDs-x in the 4000–500 cm^{-1} range (Fig. 3f) show that all WLQDs-x samples exhibit absorption bands at 826–979 cm^{-1} and 1227–1478 cm^{-1}. These

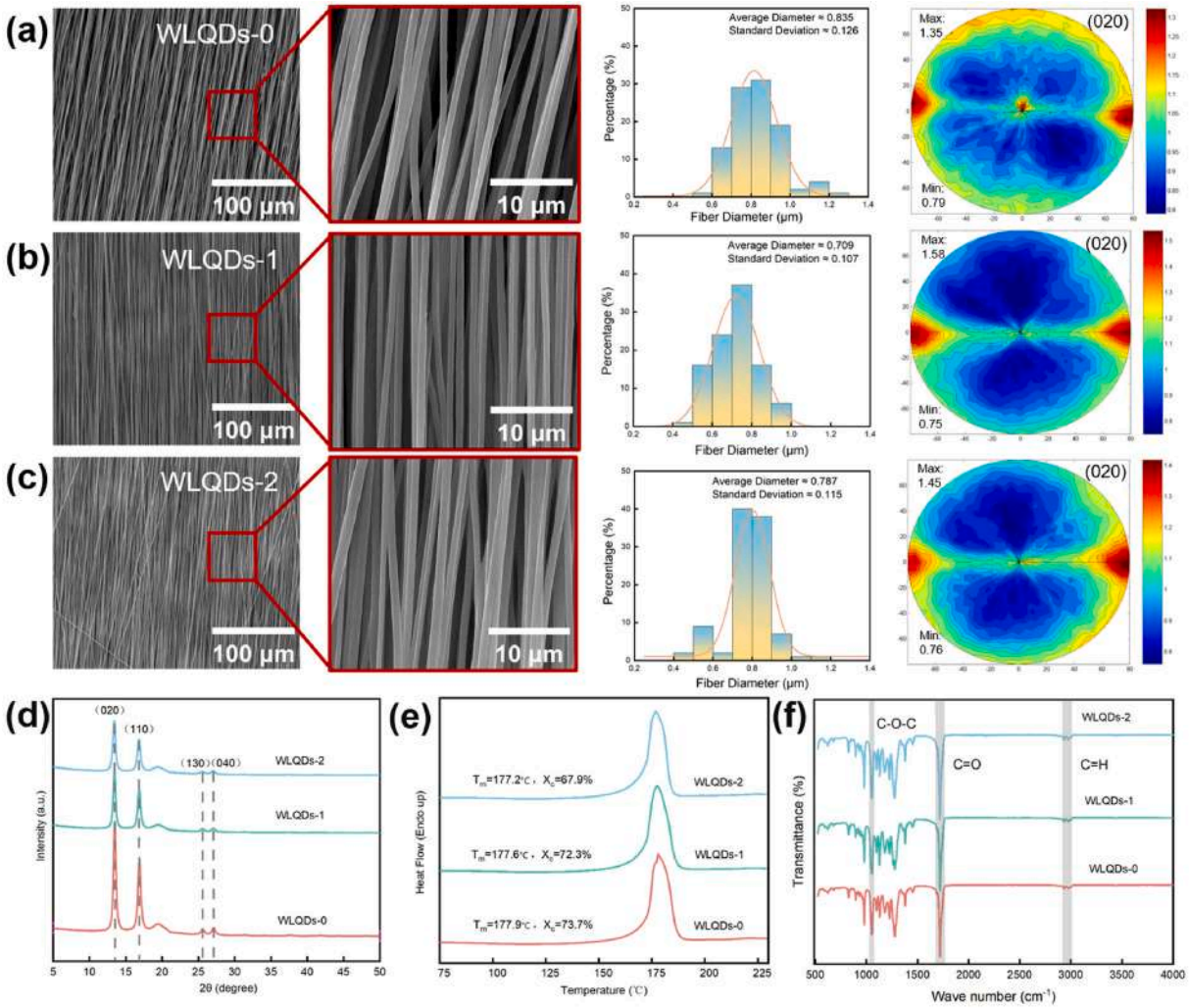


Fig. 3. (a) SEM images, diameter distribution, and XRD pole figure of the (020) crystal plane for the WLQDs-0 nanofiber membrane. (b) SEM images, diameter distribution, and XRD pole figure of the (020) crystal plane for the WLQDs-1 nanofiber membrane. (c) SEM images, diameter distribution, and XRD pole figure of the (020) crystal plane for the WLQDs-2 nanofiber membrane. (d) XRD patterns, (e) DSC curves, and (f) FTIR spectra of the WLQDs-x fiber membranes.

absorption bands correspond to C–H vibrations in PHBV [50,51]. An absorption peak at 1130 cm^{-1} is attributed to C–O vibrations in the carboxyl groups of PHBV, whilst a strong absorption peak at approximately 1720 cm^{-1} is associated with the C=O stretching vibration mode [52]. No significant changes in peak position or intensity are observed after WLQDs incorporation, indicating that no new chemical bonding is evident and that the composite is formed primarily through physical interactions.

In addition, the mechanical properties of the nanofiber membranes were also evaluated (Fig. S5). All samples exhibit tensile behavior characteristic of ductile polymers. Notably, WLQDs-1 exhibits higher tensile strength (~20.2 MPa) and higher elongation at break (~49.9%), indicating a synergistic enhancement of strength and toughness. This may be attributed to the incorporation of an appropriate amount of WLQDs, which introduces strong interfacial interactions with the PHBV and acts as physical crosslinking points. These interactions effectively promote the orientation of crystalline domains and facilitate stress transfer, thereby significantly enhancing tensile strength while mitigating the intrinsic brittleness of the polymer and improving its ductility. In contrast, excessive incorporation of WLQDs may lead to nanoparticle agglomeration, which in turn can generate stress concentration sites within the matrix, ultimately resulting in a simultaneous decrease in both tensile strength and elongation at break. Furthermore, WLQDs-x nanofiber membranes exhibit rapid degradation under composting conditions, with complete disappearance observed within four days (Fig. S6). This suggests potential applications in transient or environmentally degradable functional materials.

The structural, optical, and mechanical properties of WLQDs-x composite nanofiber membranes are summarized in Table 1. The incorporation of WLQDs affects the fiber morphology, crystallinity, luminescence efficiency, and mechanical performance of the PHBV-based nanofiber membranes.

Table 1
Structural, optical, and mechanical properties of WLQDs-x fibers.

Sample	Fiber diameter (μm)	Crystallinity (%)	Quantum yield (%)	Tensile strength (MPa)	Elongation at break (%)
WLQDs-0	0.835	73.7	-	17.9	24.8
WLQDs-1	0.709	72.3	19.94	20.2	49.9
WLQDs-2	0.787	67.9	10.27	16.8	43.2

3.3. Piezoelectric performance and electromechanical response of WLQDs-x fibers

Previous structural characterization and mechanical testing of WLQDs-x composite nanofiber membranes indicate that variations in WLQDs loading influence the microstructure of the PHBV. Variations in WLQDs content are associated with changes in the degree of orientation at both the macroscopic and microscopic scales, exhibiting a unique dual orientation pattern. This change in fiber orientation is considered to contribute to the piezoelectric response of the PHBV nanofibers. The piezoelectric behavior of PHBV originates from the orientation and reorientation of dipoles within crystalline regions under mechanical stress. Therefore, variations in microstructure are expected to affect the piezoelectric response of the composite nanofiber membranes. To evaluate the influence of WLQDs content on piezoelectric performance, a WLQDs-x-based bio-piezoelectric nanogenerator (bio-PENG) was fabricated (Fig. S1a). A sandwich configuration was employed, in which the WLQDs-x nanofiber membrane served as the active layer. Copper (Cu) electrodes were applied to both sides of the membrane, and the electrodes were further encapsulated using polyurethane (PU) tape. The open circuit voltage (V_{oc}) and short circuit current (I_{sc}) of WLQDs-x piezoelectric devices were measured under an impact force of 15 N and a frequency of 3 Hz. Both the output current and the output voltage exhibited a non-monotonic dependence on WLQDs content, increasing initially and then decreasing. The maximum values were observed for WLQDs-1, reaching 1 μA cm^{-3} and 26 V cm^{-3}, respectively (Fig. 4a). To further clarify the contribution of individual QDs components to the enhanced piezoelectric performance, two additional control samples, denoted as B-CQDs-1 and R-CISQDs-1, were prepared by incorporating 0.1 wt% B-CQDs and 0.1 wt% R-CISQDs into PHBV, respectively. R-CISQDs-1 exhibited a pronounced enhancement in both current and voltage outputs compared with pristine PHBV nanofibers, whereas B-CQDs-1 mainly improved the current output with a relatively limited effect on the voltage output. However, the overall piezoelectric performance of both single-QD systems remained inferior to that of the WLQDs-1 device, suggesting that the coexistence of B-CQDs and R-CISQDs may induce a synergistic or complementary effect in regulating the structure and piezoelectric response of PHBV nanofibers. The corresponding fiber morphology and piezoelectric outputs are provided in Figs. S7 and S8, respectively.

A comparison of the piezoelectric output of WLQDs-1 device with the reported bioorganic materials based piezoelectric nanogenerators is shown in Table S1. Based on the characterization results presented in the preceding series, we summarise the reasons for the excellent piezoelectric properties of WLQDs-1. The WLQDs-1 sample exhibits a reduced average fiber diameter accompanied by a narrower distribution, indicative of improved structural uniformity. Such homogeneity is conducive to more consistent stress transfer during deformation, thereby facilitating effective electromechanical coupling. XRD phase analysis, together with pole figure measurements and DSC results, reveals a higher degree of preferential orientation along the (020) crystal plane in WLQDs-1, while maintaining a moderate level of crystallinity. This

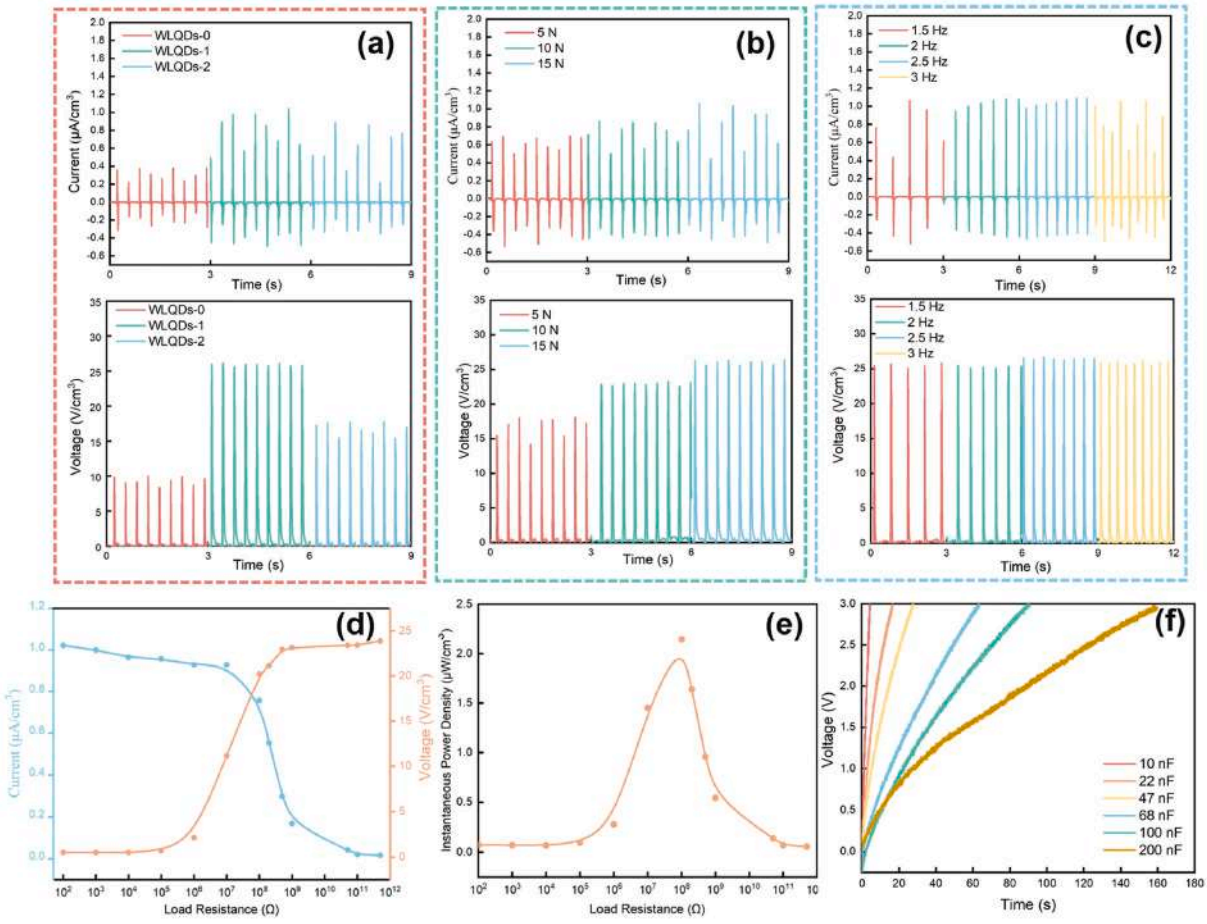


Fig. 4. (a) Short-circuit current and open-circuit voltage of the WLQDs-x device at a frequency of 3.0 Hz and an impact force of 15 N. (b) Short-circuit current and open-circuit voltage of the WLQDs-1 device at a fixed frequency of 3.0 Hz, with varying impact forces. (c) Short-circuit current and open-circuit voltage of the WLQDs-1 device at a fixed impact force of 15 N, varying with different frequencies. (d) Output voltage and current of the WLQDs-1 device under conditions of 15 N and 3 Hz, with varying external loads. (e) Power density of the WLQDs-1 device under different external loads. (f) Charging curves of the WLQDs-1 device charging different commercial capacitors.

balanced structural configuration supports the formation of piezoelectrically active crystalline domains without introducing excessive stiffness, thereby enabling reversible dipole reorientation in response to mechanical stimuli. FTIR spectra show no emergence of new characteristic peaks upon WLQD incorporation, suggesting that the interaction between WLQDs and PHBV is predominantly physical. This non-disruptive interaction preserves the intrinsic chain dynamics, which are critical for maintaining dipole mobility and thus enhancing piezoelectric responsiveness. Mechanical testing further demonstrates that WLQDs-1 exhibits superior tensile strength. This improvement is attributed to the uniform dispersion of WLQDs, which ensures efficient stress transfer while moderately constraining chain mobility. Such conditions favor the reversible distortion of pre-oriented dipoles under mechanical stimuli, leading to effective charge center separation and an enhanced piezoelectric output. The combination of uniform morphology, oriented crystalline domains, and balanced mechanical compliance facilitates more effective stress-induced dipole distortion and polarization variation, enabling efficient charge separation and ultimately leading to the superior piezoelectric performance observed for the WLQDs-1.

By varying the impact force and frequency, the influence of external conditions on the piezoelectric properties of the WLQDS-1 device was further evaluated. When the frequency was fixed at 3 Hz, both output current and voltage increased with increasing impact force (Fig. 4b). When the impact force was fixed at 15 N, varying the frequency within the tested range resulted in no significant change in piezoelectric output (Fig. 4c). Fluctuations in the output signal were observed during multiple tests on all devices (Fig. 4a–c). This may be attributed to the microstructure of the electrospun fiber membrane [53]. The viscoelastic nature of PHBV can also lead to delayed dipole response under dynamic loading [54]. In addition, slight variations at the electrode and fiber interface [55] and environmental factors, such as temperature and humidity [56], may contribute to signal variation. Despite these fluctuations, a consistent trend was observed in the average results, thereby enabling a reliable comparison of the piezoelectric performance of WLQDs-x devices under different external stimulation conditions. To evaluate the power output capability of the WLQDs-1 device, the output voltage and current were measured under different external load resistances at a fixed impact force of 15 N and a frequency of 3 Hz. As the load resistance increased, the output current decreased, while the output voltage increased and gradually approached saturation (Fig. 4d). This is consistent with the load-dependent response of piezoelectric generators and reflects the balance between charge transfer and accumulation under different resistive conditions. The instantaneous volumetric power density was calculated as a function of load resistance based on the effective volume of the active layer. The power density increased with resistance, reached a maximum, and then decreased. An optimal load resistance of approximately 100 MΩ was identified, at which the maximum power density reached 2.14 $\mu W\,cm^{-3}$. This condition corresponds to an approximate impedance matching between the device and the external circuit, which is important for efficient energy extraction. The energy storage capability of the device was evaluated by charging commercial capacitors (10–200 nF) under identical conditions. The voltage across the capacitors was recorded as a function of time (Fig. 4f), and the equivalent circuit is shown in Fig. S9(a). The charging time increased with increasing capacitance. Capacitors with smaller capacitance reached 3 V within a short time, whereas those with larger capacitance required longer charging time but stabilized within several minutes. The device was further used to drive commercial light-emitting diodes (LEDs), which could be illuminated under mechanical excitation induced by palm tapping (Fig. S9b), indicating that the device is capable of delivering useable electrical output. In addition, stable and reproducible output signals were observed over more than 10,000 loading cycles (Fig. S9c), demonstrating good operational stability. The WLQDs-1 composite nanofiber membrane not only features a straightforward fabrication process and biodegradable material properties but also exhibits excellent piezoelectric energy conversion efficiency, stable cyclic output, and practical capacitive charging capability. Furthermore, the good flexibility and biocompatibility of PHBV endow the device with application potential in fields such as human motion energy harvesting, transient wearable sensors, and self-powered medical patches. As PHBV is a biodegradable polymer, the devices can degrade harmlessly in the environment once their mission is complete, avoiding the generation of electronic waste and aligning with the development philosophy of green flexible electronics. Consequently, the WLQDs-1 piezoelectric devices prepared in this study demonstrate broad application prospects in the field of flexible transient wearable electronics.

3.4. Wearable human motion sensing applications based on WLQDs-x fibers

To further evaluate the practicality of WLQDs-1-based piezoelectric devices in wearable human motion sensing, the devices were integrated into a dance training scenario to construct a self-powered, real-time motion monitoring system. Owing to their flexibility, biocompatibility, and piezoelectric response, the sensors could be attached to various body locations to capture subtle motion changes during dance movements. The devices were positioned on the face, heels, neck, fingers, knees, and elbows to record piezoelectric output currents. The sensors responded to movement-induced deformation in each location, producing characteristic electrical signals. Eye blinking generated a transient current peak of approximately 2.5 nA, reflecting small deformations of the eye muscles (Fig. 5a). Finger and elbow flexion produced distinguishable current signals corresponding to different bending angles, enabling quantification of limb posture (Fig. 5b and c). Tiptoeing generated step like current response at the heel that corresponded to the angle of foot elevation (Fig. 5d). Larger amplitude movements, such as knee flexion and extension and head rotation, produced currents of approximately 100 to 300 nA, allowing real-time assessment of movement magnitude (Fig. 5e and f). When the device was positioned on the floor of the dance studio, three levels of movement intensity, including walking, running, and jumping, were differentiated based on output signals (Fig. S10a). The impact of a falling yoga ball from different heights produced peak currents that increased linearly with the height of fall, demonstrating a consistent and quantitative mechanical response (Fig. S10b). In addition, the device's response to musical vibrations was also evaluated. When a piano score corresponding to the dance routine was played, the current output of a WLQDs-1 device attached to the speaker base showed synchronization with the rhythm and tempo of the music (Fig. S10c). Signal peaks, troughs, and frequency variations corresponded to note duration and intensity, capturing the rhythmic features of the score. These results demonstrate that the devices can simultaneously detect mechanical signals from body movements and vibrations from background music, providing quantitative data for potential “movement–music” synchronous analysis. The WLQDs-1 devices are lightweight, flexible, and biodegradable, supporting their potential application in smart dance instruction, sports rehabilitation monitoring, and wearable human-machine interaction systems.

4. Conclusion

In summary, a WLQDs/PHBV composite nanofiber membrane with white-light emission was fabricated using biodegradable PHBV as the polymer matrix. High-speed drum collection during electrospinning promoted fiber alignment and contributed to dipole orientation. The WLQDs with CIE of (0.337, 0.305) and a quantum yield of 38.4% were obtained by physically mixing the two types of eco-friendly quantum dots, blue-emissive carbon quantum dots and red-emissive $CuInS_2$ quantum dots. After incorporating WLQDs into PHBV, the WLQDs-1 fiber membrane maintained white-light emission with a photoluminescence quantum yield of 19.94%, confirming the preservation of

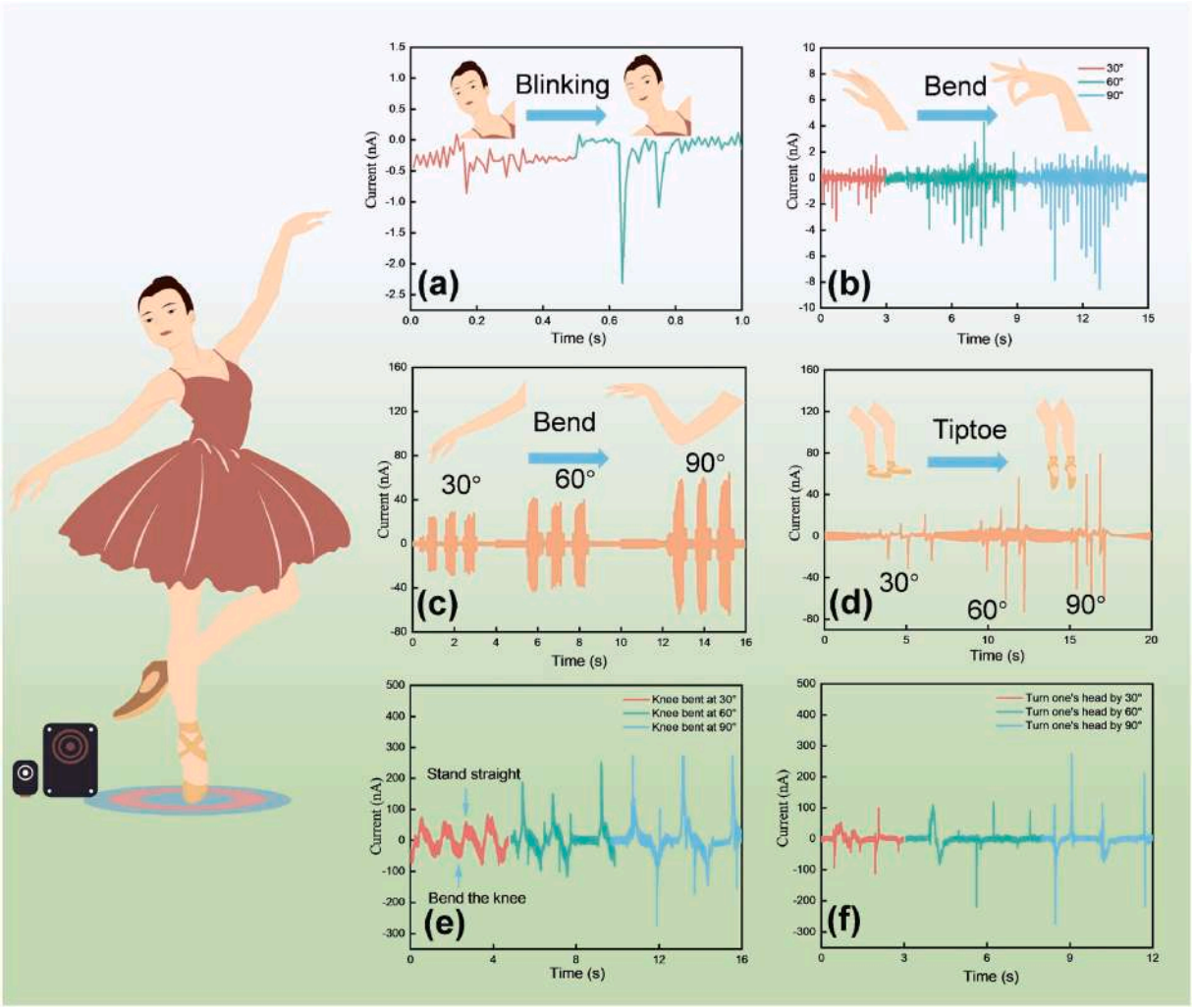


Fig. 5. (a) The piezoelectric signals are generated by a device on the face when the dancer blinks. (b) The piezoelectric signals are generated by a device adhered to the finger when the dancer's finger is bent. (c) The piezoelectric signals are generated by a device fitted to the inner elbow when the dancer bends elbow. (d) The piezoelectric signals are generated by a device installed on the heel when the dancer stands on tiptoes at different angles. (e) The piezoelectric signals are generated by a device at the knee when the dancer bends knee joint. (f) The piezoelectric signals are generated by a device attached to the neck when the dancer turns head.

the optical functionality following fiber formation. Compared with pristine PHBV, the WLQDs-1 fiber membrane showed slightly reduced crystallinity but enhanced orientation of the (020) crystal plane. Improved mechanical performance was also observed. Under periodic impact at 15 N and 3 Hz, the WLQDs-1 based piezoelectric device exhibited a short-circuit current density of 1 $\mu A\,cm^{-3}$ and an open-circuit voltage density of 26 $V\,cm^{-3}$. These values were higher than the corresponding values measured for the pristine PHBV-based device as well as for the WLQDs/PHBV-based device with a higher WLQDs content. The enhanced piezoelectric response was associated with the combined effect of moderate crystallinity and increased crystal orientation. The WLQDs-1 membrane was further applied in wearable motion sensing. When attached to different parts of the human body, the device enabled real-time sensitive detection of motion signals during dance movements. The WLQDs/PHBV composite nanofiber membrane combines white-light emission, piezoelectric response, mechanical stability, and biodegradability. These features suggest potential applications in motion sensing, wearable electronics, and transient electronic systems.

Although the present work has successfully integrated white-light emission and piezoelectric sensing functionalities into a single bio-composite fiber material, these two functionalities are currently demonstrated separately, and their synergistic interactions have not yet been explored. Developing a coupled "emission + piezo-sensing" system, in which mechanical stimuli can be translated into real-time optical feedback, represents an important future direction. Future efforts will focus on constructing a multifunctional integrated platform that combines optical visualization with piezoelectric sensing responses, enabling advanced wearable and sustainable electronic applications.

CRediT authorship contribution statement

Juan Li: Writing – original draft, Validation, Methodology, Investigation, Conceptualization. **Chu Pan:** Investigation. **Biyao Huang:** Investigation. **Zhipei Xia:** Investigation. **Jiashun Wen:** Investigation. **Xuhang Lu:** Investigation. **Weiqing Yang:** Writing – review & editing, Supervision, Resources. **Jun Lu:** Writing – review & editing, Supervision, Resources, Funding acquisition, Conceptualization.

Declaration of competing interest

The authors declare that they have no known competing financial interests or personal relationships that could have appeared to influence the work reported in this paper.

Acknowledgements

This work was financially supported by National Natural Science Foundation of China (No. 52073237).

Appendix A. Supplementary data

Supplementary data to this article can be found online at https://doi.org/10.1016/j.coco.2026.102982.

Data availability

Data will be made available on request.

References

[1] H. Xiang, R. Wang, J. Chen, F. Li, H. Zeng, Research progress of full electroluminescent white light-emitting diodes based on a single emissive layer, Light Sci. Appl. 10 (2021) 206.
[2] L. Ying, C.L. Ho, H. Wu, Y. Cao, W.Y. Wong, White polymer light-emitting devices for solid-state lighting: materials, devices, and recent progress, Adv. Mater. 26 (2014) 2459–2473.
[3] J. Cho, J.H. Park, J.K. Kim, E.F. Schubert, White light-emitting diodes: history, progress, and future, Laser Photon. Rev. 11 (2017) 1600147.
[4] S. Zhao, J. Sun, Z. Qin, Y. Li, H. Yu, G. Wang, X. Gu, K. Pan, Janus-structural AIE nanofiber with white light emission and stimuli-response, Small 18 (2022) 2201117.
[5] Z. Qin, P. Zhang, Z. Wu, M. Yin, Y. Geng, K. Pan, Coaxial electrospinning for flexible uniform white-light-emitting porous fibrous membrane, Mater. Des. 147 (2018) 175–181.
[6] M. Yang, Y. Yuan, F. Shen, W.G. Li, Y. Jiang, A. Wang, L. Li, G. Liu, Y.X. Chen, Q. Xu, H. Pang, T. Tian, Synergistic chlorine source regulation and defect-passivation strategy for stable blue-emitting perovskite films toward non-invasive jaundice therapy, Adv. Opt. Mater. 14 (2026) e02560.
[7] B. Xu, X.Q. Peng, H. Zhong, L.F. Wang, X. Jin, J.K. Bai, Q.H. Li, Incorporating Sb (III) and Bi (III) ions into $Cs_2AgNaInCl_6$ perovskite toward efficient white-light emission with high color rendering index, Chem. Eng. J. 499 (2024) 155510.
[8] Q.H. Li, F.F. Ma, X.Q. Peng, T.F. Gao, B. Xu, L.T. Huang, J.K. Bai, Q.P. Li, W. F. Zhao, Dynamic color-tunable luminescence in lead-free perovskites by asymmetric energy transfer and excitation-dependent dual self-trapped excitons emission, Chem. Eng. J. 521 (2025) 166819.
[9] Z. Qin, S. Zhao, X. Fang, B. Zhao, J. Deng, K. Pan, Flexible, ultra-light, and 3D designed white-light-emitting nanofiber aerogel, Adv. Funct. Mater. 32 (2022) 2109240.
[10] X. Huang, L. Jin, C. Wang, Y. Xu, Z. Peng, M. Xie, C. Zhang, W. Yang, J. Lu, Electrospun luminescent piezo webs as self-powered sensing platform for small accelerations at low frequency, Compos. Commun. 20 (2020) 100348.
[11] K. Chang, M. Guo, L. Pu, J. Dong, L. Li, P. Ma, Y. Huang, T. Liu, Wearable nanofibrous tactile sensors with fast response and wireless communication, Chem. Eng. J. 451 (2023) 138578.
[12] B. Subeshan, A. Atayoe, E. Asmatulu, Machine learning applications for electrospun nanofibers: a review, J. Mater. Sci. 59 (2024) 14095–14140.
[13] J.X. Liu, X.D. Chai, X.L. Zhang, X.C. Jia, H.Z. Yao, J.L. Fu, Review on functional electrospun nanofibers: theory, application and fabrication, Mater. Sci. Eng. B 307 (2024) 117488.
[14] J. Wei, K. Yu, Y. Yu, S. Li, H. Yu, B. Li, Y. Cui, Q. Abdul, Q. Chen, Z. Hao, Q. Xiao, Photo-reduced TiO_2@WO_3 electrospun nanofibers for efficient SERS and photoelectrochemical performances, Compos. Commun. 46 (2024) 101847.
[15] L. Liu, Y. Liu, J. Min, Q. Ding, Y. Fan, J. Yu, W. Jiang, Nanofiber derived MXene composite paper for electromagnetic shielding and thermal management, Compos. Commun. 48 (2024) 101935.
[16] X. Zhong, Y. Pan, Z. Feng, Z.-B. Shao, J. Qiu, L. Zhu, Rice straw-based cellulose nanofiber reinforcing polyvinyl alcohol antibacterial film through electrospinning, Compos. Commun. 49 (2024) 101972.
[17] M. Xu, X. Yao, Y. Wang, H. Liu, W. Yang, P. Zhang, Electrospun miRNA-21@ doxycycline core-sheath nanofibers for a synergistic treatment of diabetic wounds, Compos. Commun. 53 (2025) 102239.
[18] N. Yao, F. Wang, S. Zhang, J. Yu, B. Ding, One-step fabrication of mechanically robust and fluorine-free nanofiber membranes for waterproofness and breathability, Compos. Commun. 56 (2025) 102396.
[19] S. Wu, Y. Zhao, J. Wang, X. Zhao, W. Zhai, X. Zhu, P. Wan, M. Cui, L. Gao, K. Dai, C. Liu, C. Shen, All-nanofiber self-powered electronic skin with electrospinning humidity-controlled structure for human muscle detection during fitness, Compos. Commun. 57 (2025) 102421.
[20] J. Xue, T. Wu, Y. Dai, Y. Xia, Electrospinning and electrospun nanofibers: methods, materials, and applications, Chem. Rev. 119 (2019) 5298–5415.
[21] Y. Ding, H. Hou, Y. Zhao, Z. Zhu, H. Fong, Electrospun polyimide nanofibers and their applications, Prog. Polym. Sci. 61 (2016) 67–103.
[22] Y. Cho, J.W. Baek, M. Sagong, S. Ahn, J.S. Nam, I.D. Kim, Electrospinning and nanofiber technology: fundamentals, innovations, and applications, Adv. Mater. 37 (2025) 2500162.
[23] F. Li, D. Lin, Z. Chen, Z. Cheng, J. Wang, C.C. Li, Z. Xu, Q. Huang, X. Liao, L. Q. Chen, T.R. Shrout, S.J. Zhang, Ultrahigh piezoelectricity in ferroelectric ceramics by design, Nat. Mater. 17 (2018) 349–354.
[24] Y.M. You, W.Q. Liao, D. Zhao, H.Y. Ye, Y. Zhang, Q.H. Zhou, X.H. Niu, J.L. Wang, P.F. Li, D.W. Fu, Z.M. Wang, S. Gao, K.L. Yang, J.M. Liu, J.Y. Yan, Y. Yan, R. G. Xiong, An organic-inorganic perovskite ferroelectric with large piezoelectric response, Science 357 (2017) 306–309.
[25] Y. Liu, H. Aziguli, B. Zhang, W.H. Xu, W.C. Lu, J. Bernholc, Q. Wang, Ferroelectric polymers exhibiting behaviour reminiscent of a morphotropic phase boundary, Nature 562 (2018) 96–100.
[26] S. Anwar, M. Hassanpour Amiri, S. Jiang, M.M. Abolhasani, P.R.F. Rocha, K. Asadi, Piezoelectric nylon-11 fibers for electronic textiles, energy harvesting and sensing, Adv. Funct. Mater. 31 (2021) 2004326.
[27] L. Kaniuk, U. Stachewicz, Development and advantages of biodegradable PHA polymers based on electrospun PHBV fibers for tissue engineering and other biomedical applications, ACS Biomater. Sci. Eng. 7 (2021) 5339–5362.
[28] S. García-Chumillas, T. Guerrero-Murcia, M. Nicolás-Liza, F. Monzó, A. Simica, L. Simó-Cabrera, R.M. Martínez-Espinosa, PHBV cycle of life using waste as a starting point: from production to recyclability, Front. Mater. 11 (2024) 1405483.
[29] J. Hu, Y. Sun, A.A. Aryee, L. Qu, K. Zhang, Z. Li, Mechanisms for carbon dots-based chemosensing, biosensing, and bioimaging: a review, Anal. Chim. Acta 1209 (2022) 338885.
[30] H. Li, X. Yan, D. Kong, R. Jin, C. Sun, D. Du, Y. Lin, G. Lu, Recent advances in carbon dots for bioimaging applications, Nanoscale Horiz. 5 (2020) 218–234.
[31] S. Pandit, T. Banerjee, I. Srivastava, S. Nie, D. Pan, Machine learning-assisted array-based biomolecular sensing using surface-functionalized carbon dots, ACS Sens. 4 (2019) 2730–2737.
[32] H. Wang, S. Deng, X. Liu, H. Liu, R. Gao, B. Zeng, Y. Xu, G. Chen, W. Luo, C. Yuan, L. Dai, Waterborne epoxy composite coating containing N,S-doped carbon dots for enhancing corrosion resistance, Compos. Commun. 48 (2024) 101888.
[33] X. Yang, Y. Li, D. Yue, R. Li, H. Song, Facile synthesis of NH_2-MIL-53(Al)@BiOBr@ CQDs ternary heterostructure photocatalyst for degradation of ciprofloxacin in water, Compos. Commun. 50 (2024) 102028.
[34] L. Zhang, W. Wang, P. Jin, Z. Sun, Y. Zhan, B. Jiang, Reactive carbon dots/ polysiloxane composites cross-linked silicone resin adhesives for stable white LED constructing, Compos. Commun. 53 (2025) 102172.
[35] J. Chen, X. Cao, W. Fan, H. Ma, X. Jiang, Z. Sun, Y. Zhan, Full-color emissive organosilicon-coated carbon dots microspheres for latent fingerprint development with level 3 details, Compos. Commun. 54 (2025) 102277.
[36] Z. Liu, X. Liu, L. Dai, J. Sun, J.-J. Wang, C. Qin, L. Dai, G. Chen, Sustainable spent coffee ground carbon dots/polylactic acid fiber green composites with superior damp heat resistance, Compos. Commun. 56 (2025) 102388.
[37] X. Guan, L. Zhang, S. Lai, J. Zhang, J. Wei, K. Wang, W. Zhang, C. Li, J. Tong, Z. Lei, Green synthesis of glyco-$CuInS_2$ QDs with visible/nir dual emission for 3D multicellular tumor spheroid and in vivo imaging, J. Nanobiotechnol. 21 (2023) 118.
[38] Z. Liu, Y. Lai, J. Li, Z. Xia, L. Lu, C. Wang, B. Huang, C. Pan, J. Wen, W. Yang, J. Lu, Natural biopolymer/$CuInS_2$ quantum dot-based red emissive, physically transient, and dynamically self-polarized piezoelectrets, Compos. Commun. 48 (2024) 101919.
[39] Z. Zhe, Cellulose nanocrystals as green fillers to improve crystallization and hydrophilic property of poly (3-hydroxybutyrate-co-3-hydroxyvalerate), Prog. Nat. Sci. 21 (2011) 478–484.
[40] R.S. Yang, Y. Qin, C. Li, L.M. Dai, Z.L. Wang, Characteristics of output voltage and current of integrated nanogenerators, Appl. Phys. Lett. 94 (2009) 022905.
[41] S.Y. Xu, Y.W. Yeh, G. Poirier, M.C. McAlpine, R.A. Register, N. Yao, Flexible piezoelectric PMN-PT nanowire-based nanocomposite and device, Nano Lett. 13 (2013) 2393–2398.
[42] X. Kang, R. Zhao, Q. Chen, Y. Yuan, S. Liu, K. Feng, C. Mao, J. Wang, Mechanically driven polarization for wireless and bioadaptive piezoelectric cardiac patches, Cell biomater 2 (2026) 100299.
[43] B. Zaarour, L. Zhu, X. Jin, Controlling the surface structure, mechanical properties, crystallinity, and piezoelectric properties of electrospun PVDF nanofibers by maneuvering molecular weight, Soft Mater. 17 (2019) 181–189.
[44] M. Zhang, C. Liu, B. Li, Y. Shen, H. Wang, K. Ji, X. Mao, L. Wei, R. Sun, F. Zhou, Electrospun PVDF-based piezoelectric nanofibers: materials, structures, and applications, Nanoscale Adv. 5 (2023) 1043–1059.
[45] K. Ren, Y. Shen, Z.L. Wang, Piezoelectric properties of electrospun polymer nanofibers and related energy harvesting applications, Macromol. Mater. Eng. 309 (2024) 2300307.
[46] J. Chen, C. Ayranci, T. Tang, Piezoelectric performance of electrospun PVDF and PVDF composite fibers: a review and machine learning-based analysis, Mater. Today Chem. 30 (2023) 101571.
[47] D.X. Ji, Y.A. Lin, X.Y. Guo, B. Ramasubramanian, R.W. Wang, N. Radacsi, R. Jose, X.H. Qin, S. Ramakrishna, Electrospinning of nanofibres, Nat. Rev. Methods Primers 4 (2024) 1.
[48] P.P. Putra, S. Akasaka, Y. Konosu, S. Zhang, A. Tanioka, H. Matsumoto, Structure–Piezoelectric property relationships of thin films composed of electrospun aligned poly (vinylidene fluoride) nanofibers, Nanomaterials 14 (2024) 491.
[49] S. Gee, B. Johnson, A.L. Smith, Optimizing electrospinning parameters for piezoelectric PVDF nanofiber membranes, J. Membr. Sci. 563 (2018) 804–812.
[50] K.S. Jack, S. Velayudhan, P. Luckman, M. Trau, L. Grondahl, J. Cooper-White, The fabrication and characterization of biodegradable HA/PHBV nanoparticle–polymer composite scaffolds, Acta Biomater. 5 (2009) 2657–2667.

[51] L. Amaro, D.M. Correia, P.M. Martins, G. Botelho, S.A.C. Carabineiro, C. Ribeiro, S. Lanceros-Mendez, Morphology dependence degradation of electro-and magnetoactive poly (3-hydroxybutyrate-co-hydroxyvalerate) for tissue engineering applications, Polymers 12 (2020) 953.
[52] B. Fei, C. Chen, H. Wu, S. Peng, X. Wang, L. Dong, Quantitative FTIR study of PHBV/bisphenol A blends, Eur. Polym. J. 39 (2003) 1939–1946.
[53] S. Wang, Y. He, L. Peng, P. Jiang, H. Wang, H. Chang, T. Lin, Source dependence of polyacrylonitrile electrospun nanofibers on piezoelectric response, J. Mater. Chem. A 13 (2025) 19782–19794.
[54] M. Smith, S. Kar-Narayan, Piezoelectric polymers: theory, challenges and opportunities, Int. Mater. Rev. 67 (2022) 65–88.
[55] L.X. Wu, S.J. Ma, M.J. Li, X.L. Zhang, G. Zheng, Z. Liang, R. Li, H. Dong, J. Zhang, Y.Z. Long, Interfacial charge transfer mechanism and output characteristics of identical-material triboelectric nanogenerators, Nanomaterials 15 (2025) 708.
[56] A.A. Fajingbesi, F.T. Omigbodun, O. Odesanya, E.O. Oluwabiyi, E.A. Adeola, A. A. Onif, P. Adeyekun, Colloid-engineered hybrid nanogenerators with humidity-stable output and lower carbon footprint for urban energy harvesting, Colloids Surf. A Physicochem. Eng. Asp. 731 (2025) 139031.